

# Internal flow measurements of drop impacting a solid surface

S. Santosh Kumar<sup>1,2</sup> · Ashish Karn<sup>1</sup> · Roger E. A. Arndt<sup>1</sup> · Jiarong Hong<sup>1,2</sup>

Received: 18 February 2016 / Revised: 27 June 2016 / Accepted: 15 December 2016 / Published online: 3 February 2017  
© Springer-Verlag Berlin Heidelberg 2017

**Abstract** Understanding the fundamental physical process involved in drop impacts is important for a variety of engineering and scientific applications. Despite exhaustive research efforts on the dynamics of drop morphology upon impact, very few studies investigate the fluid dynamics induced within a drop upon impact. This study employs planar particle image velocimetry (PIV) with fluorescent particles to quantify the internal flow field of a drop impact on a solid surface. The image distortion caused by the curved liquid–air interface at the drop boundary is corrected using a ray-tracing algorithm. PIV analysis using the corrected images has yielded interesting insights into the flow initiated within a drop upon impact. Depending on the pre-impact conditions, characterized by impact number, different vortex modes are observed in the recoil phase of the drop impact. Further, the strength of these vortices and the kinetic energy of the internal flow field have been quantified. Our studies show a consistent negative power law correlation between vortex strength, internal kinetic energy and the impact number.

## 1 Introduction

Understanding the fundamental physical process involved in drop impacts is important for a variety of engineering

applications, such as ink-jet printing, rapid spray cooling of hot surfaces, quenching of aluminum alloys and steel, and fuel injection in internal combustion engines (Yarin 2006). It also plays a significant role in scientific studies including soil erosion due to rainfall (Sharma et al. 1995), the analysis of blood splatter patterns in criminal forensic investigations (Hulse et al. 2007; Attinger et al. 2013) and asteroid impact modeling (Zhao et al. 2015).

As reviewed by Yarin (2006), the drop impacts can be divided into two categories: substrate deposition and splashing. For substrate deposition, the impact process generally involves four phases: pre-impact, spreading, recoil, and decay. The pre-impact phase begins at the point of drop ejection from the syringe and ends at the point of impact. Upon impact, the drop spreads radially outwards, forming a very thin flattened disk shape and momentarily coming to rest. The recoil phase occurs after the spreading phase, in which the spread of the drop moves inwards and upwards to reach a maximum height and then recoil back downwards. This oscillation gradually decays under the effect of dissipative forces. The substrate deposition dynamics of drops is generally characterized by a number of dimensionless groups including the Reynolds number ( $Re = \rho D_0 U_0 / \mu$ ), Weber number ( $We = \rho D_0 U_0^2 / \sigma$ ), and the impact number ( $P = We / Re^{4/5}$ , where  $\rho$ ,  $\sigma$ ,  $\mu$ ,  $D_0$  and  $U_0$  are the density, surface tension coefficient, dynamic viscosity, pre-impact diameter and velocity of the liquid drop, respectively). Specifically, the impact number, which represents the relative significance of surface tension limited drop spreading and viscosity limited drop spreading has been employed by previous studies (such as Clanet et al. 2004) to characterize the spreading dynamics of the substrate deposition.

A variety of experimental techniques, including conventional high speed imaging, shadowgraphy, interferometry and X-ray imaging, have been employed in the study

✉ Jiarong Hong  
jhong@umn.edu

<sup>1</sup> Saint Anthony Falls Laboratory, 2 Third Avenue,  
Minneapolis, MN 55414, USA

<sup>2</sup> Department of Mechanical Engineering, University  
of Minnesota, 111 Church Street SE, Minneapolis,  
MN 55455, USA

of drop impacts. However, the majority of these studies are focused on the dynamics occurring at drop surfaces, such as spreading, recoil, splashing and air entrapment, and its relationship with pre-impact conditions characterized by different dimensionless groups. For example, conventional high speed imaging was employed in the study of the splashing threshold (Yarin and Weiss 1995) and the maximum spreading (Clanet et al. 2004) of impacting drops. Li and Thoroddsen (2015) applied high speed, two-color interferometry to study the evolution of the air layer under an impacting drop. X-ray imaging was adopted by a number of recent studies on the air entrapment (Lee et al. 2012) and jet formation (Zhang et al. 2012; Thoraval et al. 2013; Agbaglah et al. 2015; Lee et al. 2015) during the impact process. For instance, Lee et al. (2012) investigated the capillary wave dynamics between the liquid drop and the air entrapped upon drop impact on a solid surface. Thoraval et al. (2013) observed von Karman vortex street between the drop and the liquid surface, which is found to significantly affect the jet formation during impact.

Further, a large number of numerical studies have investigated the spreading and splashing dynamics of drop impacts on solids, liquid coated interfaces, and on liquid pools. For example, Rieber and Frohn (1999) conducted direct numerical simulations of splashing based on the Navier–Stokes equation and successfully predicted the extension dynamics of the splashing lamella. Weiss and Yarin (1999) used a boundary integral method to study drop impacts on liquid films and predicted disk-like jet formations between the drop and the liquid film. Additionally, Thoraval et al. (2012) through high resolution direct numerical simulations, investigated these jets and found the presence of a von Karman vortex street between the drop and the liquid pool.

Despite such exhaustive research efforts, very few studies investigate the fluid dynamics induced within a drop upon impact. Using particle image velocimetry (PIV) and refractive index matching technique, Mohamed-Kassim and Longmire (2003) conducted some exploratory study on the internal flow during the impact of a drop onto a

liquid–liquid interface and demonstrated the presence of circulation within the drop. However, such internal flows have not been thoroughly investigated, particularly under the settings of drop impacting a solid surface. Further, the presence of any internal motion within the drop has been ignored in the development of models for drop pinch-off and splashing. It is hypothesized that the internal motion, initiated within a drop upon impact, may play an important role in the evolution of the drop’s morphology. Thus, in this study, we focus on visualizing and quantifying this internal motion. In this paper, we report a systematic experimental study on the internal flow fields during substrate deposition of drop on a solid surface. This paper is structured as follows: Sect. 2 provides a description of the experimental setup and techniques. The results from our study are presented and discussed in Sect. 3, which is followed by a conclusion in Sect. 4.

## 2 Experimental methodology

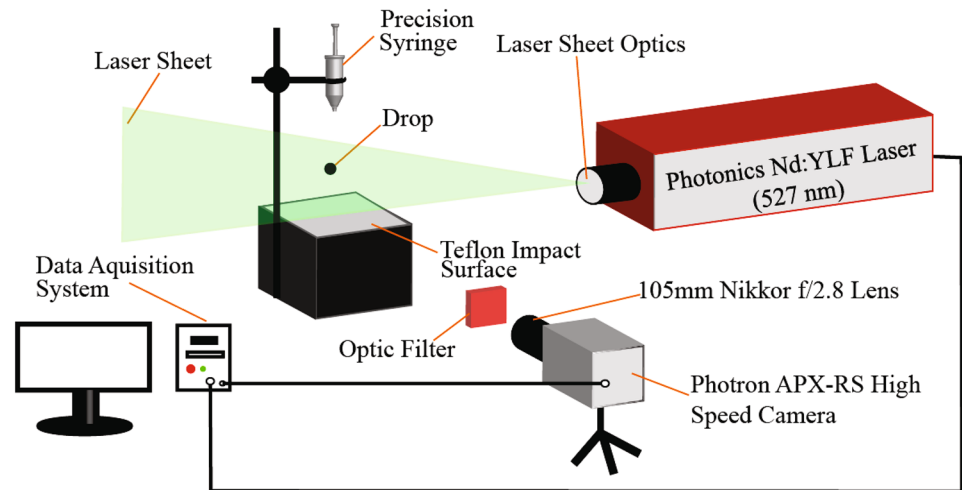
Time-resolved planar particle image velocimetry (PIV) with fluorescent tracer particles is employed to quantify the internal flow field of a drop impacting on a solid surface. As shown in Fig. 1, the experimental setup includes a drop injection system, a drop impact surface, an illumination system, an imaging and data acquisition system. The drop injection system consists of a precision syringe in combination with needles of various diameters. The syringe is mounted on a rigid fixture which is calibrated to ensure orthogonal impacts. The drops are produced using a mixture of water and glycerin as shown in Table 1. Different compositions of water and glycerin are used to generate drops of a wide range of physical properties (i.e., diameter, viscosity, etc.) and the corresponding pre-impact conditions characterized by aforementioned dimensionless groups. The fluorescent particles (5  $\mu\text{m}$  diameter; Cospheric Inc.) had a peak excitation wavelength of  $\lambda_{\text{abs}} = 575$  nm and a peak emission wavelength of  $\lambda_{\text{emit}} = 607$  nm. The particles have reasonably

**Table 1** The physical properties and the corresponding experiment conditions for drops of different mixtures

Mixture number	Glycerin /water (v/v%)	Dynamic viscosity, $\mu$ ( $\times 10^{-3}$ Pa s)	Density ( $\text{kg/m}^3$ )	Surface tension, $\sigma$ (N/m)	$D_0$ (mm)	$We$	$Re$ ( $\times 10^3$ )	$P$
I	0/100	1.00	998.2	0.073	4.4–5.3	9–141	1.7–7.0	0.02–0.11
II	10/90	1.31	1023.7	0.071	4.5–5.6	30–222	2.4–7.0	0.05–0.18
III	30/70	2.50	1073.9	0.066	3.8–4.3	30–282	1.2–3.6	0.10–0.39
IV	50/50	5.00	1127.1	0.067	3.5–3.8	40–261	0.6–1.7	0.21–0.67

Note that the experiments are conducted at 21  $^{\circ}\text{C}$  and ambient pressure of 0.101 MPa. Mixture properties have been taken from Glycerine Producers’ Association (1963)

**Fig. 1** A schematic of the experimental setup



good traceability, as quantified by their Stokes number, i.e.,  $Stk = \rho_p d_p^2 U_0 / (18 D_0 \mu) = 1.5 \times 10^{-4}$ , where  $\rho_p$  and  $d_p$  are the particle density ( $1300 \text{ kg/m}^3$ ) and the diameter, respectively. Note that in the expression of Stokes number the characteristic fluid time scale is approximated using the pre-impact velocity ( $U_0$ ) and the drop diameter ( $D_0$ ). The seeding density is chosen to ensure sufficient particle pairs in each PIV interrogation window as discussed later. A square solid block coated with Teflon serves as the hydrophobic impacting surface. A thin silicone oil ( $\nu = 10^{-5} \text{ m}^2/\text{s}$ ,  $\rho = 930 \text{ kg/m}^3$ ) coating is applied on the Teflon layer to further eliminate surface imperfections. Note that the thickness of the oil coating is just sufficient to ensure a perfectly flat impact surface. The impacting surface is placed on an optical bench to minimize the surface vibrations during the impact process. To ensure the same surface condition, a fresh surface is prepared for each set of impact experiments. The illumination source consists of a Photonics high-speed Q-switch Nd:YLF laser with a peak wavelength of 527 nm, a maximum intensity of 30 mJ/pulse at 1 kHz, and a pulse width of 150 ns. In our experiments, a pulsed light sheet of 500  $\mu\text{m}$  thickness and 3 kHz repetition rate, produced by a series of cylindrical and spherical lenses, illuminates the drop's plane of symmetry. The fluorescent particle images are captured by a Photron APX-RS high-speed digital camera operating with a  $1\text{k} \times 1\text{k}$  pixel sensor at 3 kHz acquisition rate. A high pass optic filter, with a cut-off wavelength of 590 nm is used to minimize ambient light and reflection from the illumination source ( $\lambda = 527 \text{ nm}$ ) and highlight the signals from the fluorescent particles. A micro Nikkor 105 mm f/2.8 imaging lens is used to obtain 1:1 magnification, yielding a  $17.4 \text{ mm} \times 17.4 \text{ mm}$  field of view and a spatial resolution of  $17 \mu\text{m}/\text{pixel}$ , sufficient to capture the entire range of the drop's motion.

The quantitative visualization and velocity field measurements within the drop as it impacts the solid surface is hindered by geometrical optical distortion caused by refraction of light at the drop boundary. To correct this distortion, an algorithm based on Minor et al. (2007) has been developed which we illustrate in Fig. 2a–c using a synthetic distortion field and a rectangular test grid. The algorithm employs the principles of optical ray tracing to derive a mapping function between the image plane and the object plane. The first step towards the correction process involves the accurate identification of the droplet edge through iterative thresholding, using the change in segmented area as the optimization metric. A Savitzky–Golay filter is applied to produce smooth drop edge profile with sub-pixel resolution (Fig. 2d). As shown in Fig. 2d, a typical 2D measured profile of the drop during impact experiments has a slight asymmetry between left and right side of the drop, which prevents us from using axisymmetric assumption to obtain the 3D drop interface. To cope with this limitation, we compute the full 3D surface by linearly interpolating between the left and right sides in a spherical coordinate system (Fig. 2e). Once the geometry of the surface is resolved, the normal vector ( $N$ ) at each location on the 3D drop surface can be obtained.

As a light ray traverses from the object plane to the image sensor, it is refracted by the drop surface. The angle of incidence to the surface ( $\psi_d$ ), and the angle of refraction ( $\psi_a$ ), are related by Snell's Law of refraction

$$n_d \sin \psi_d = n_a \sin \psi_a \quad (1)$$

where  $n_a$  and  $n_d$  are the refractive indices of air and the drop, respectively. In particular, the angle of incidence is the angle between the normal to the surface ( $N$ ) and the normal to the image sensor ( $-\hat{k}$ )

$$\cos(\psi_a) = N \cdot (-\hat{k}) \quad (2)$$

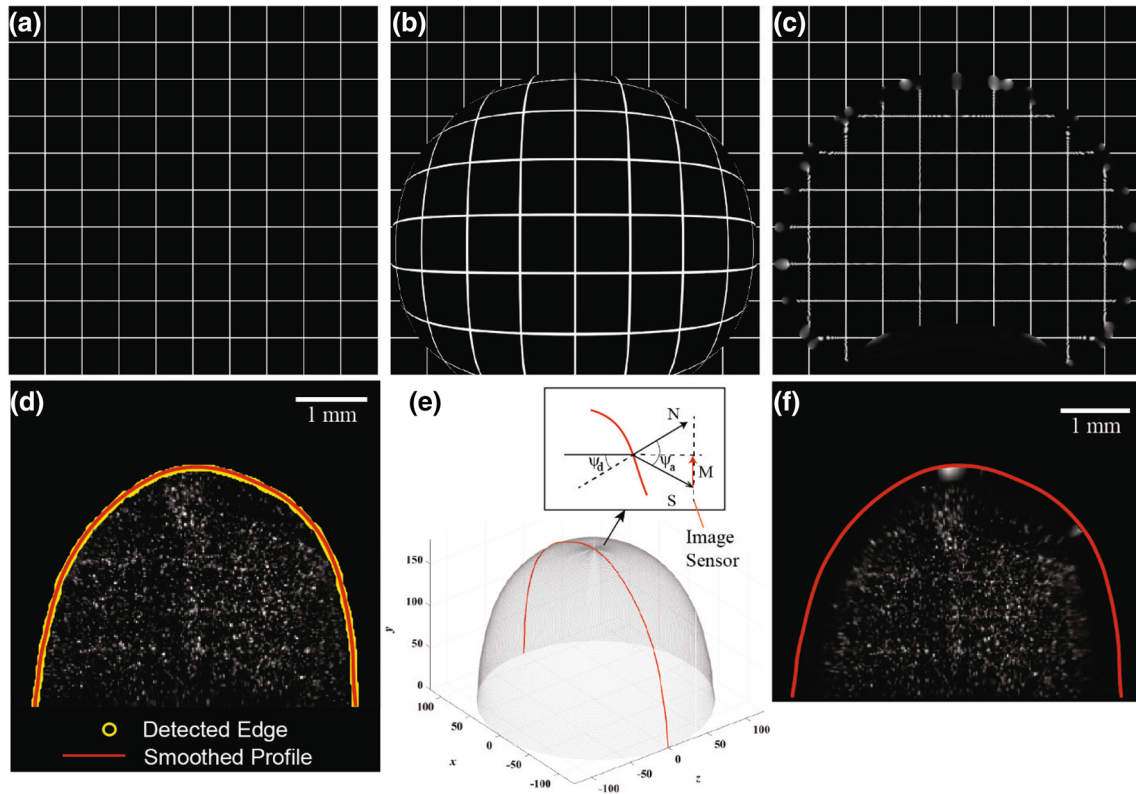


**Fig. 2** **a** Synthetic test grid image. **b** Image with a synthetic distortion field. **c** Distortion corrected image showing regions where data is completely recovered and where no recovery is possible (near the interface and close to the surface). **d** Recorded image with detected

edge profile. Note the slight asymmetry in the droplet profile. **e** Three dimensional surface profile computed through linear interpolation with an *inset* showing light ray refraction at the interface. **f** Distortion corrected image with detected surface profile

where  $\hat{k}$  is the unit vector in the  $z$  direction. The subsequent mapping function,  $M = (M_x, M_y, M_z)$ , can be calculated as:

$$M = -\hat{k} - \tan(\psi_a - \psi_d) \frac{\hat{k} \times (N \times \hat{k})}{|\hat{k} \times (N \times \hat{k})|} \quad (3)$$

Thus, given  $(x_s, y_s)$  as the location of a pixel on the distorted image, the undistorted pixel's location  $(x_0, y_0)$  can be expressed as:

$$x_0 = x_s - \frac{z_s M_x}{M_z} \quad (4)$$

$$y_0 = y_s - \frac{z_s M_y}{M_z} \quad (5)$$

Note that  $z_s$  is the corresponding  $z$  coordinate of  $(x_s, y_s)$  on the 3D reconstruction of the drop surface. This algorithm is employed over the entire recoil phase to correct the distortion before proceeding to PIV measurements. Figure 2f illustrates the effect of the distortion correction algorithm applied to a sample image where we see a migration

of the pixels towards the center of the droplet. The curvature of the droplet prevents the recovery of information close to the interface. Once the images are corrected, we calculate the velocities using cross-correlation technique.

To mask the drop for PIV cross correlation, an erosion operation, over 10 pixels, is applied to the corrected images. Additionally, a sliding background subtraction of 20 pixels was performed to enhance the particle images. The masked portion of these images (i.e., the particle field inside the drop) is processed using an adaptive multi-pass cross-correlation algorithm in *LaVision Davis 8.2* software, starting from  $48 \times 48$  pixel interrogation window to  $32 \times 32$  pixel interrogation window, with a 75% overlap. It has been ensured that even the smallest interrogation window (i.e.,  $32 \times 32$  pixel) had 10–15 particles to yield robust cross-correlation. A median filter is used to remove vectors whose difference to the median is greater than twice of the standard deviation of its neighbors. The missing vectors are then interpolated. A median filter of width corresponding three consecutive frames (i.e., 1 ms in time) is applied to smooth out spurious velocity fluctuations in the instantaneous vector field. The pre-impact drop diameter is defined as the

mean equivalent diameter of the droplet over the complete falling phase. Displacement of the drop centroid is used to calculate the drop velocity during the pre-impact phase through a quadratic curve fit.

### 3 Results and discussion

In this section, we report the evolution of the internal velocity and vorticity fields at various phases of substrate deposition of a drop on a solid surface and provide corresponding discussion on the results. The variation of the internal vortex patterns depending on different pre-impact conditions is further investigated. The dependence of the internal kinetic energy and the internal vorticity on pre-impact conditions specifically due to the fluid motions inside the drop is also quantified.

#### 3.1 Evolution of internal velocity and vorticity field during drop impact

Figure 3 shows the motion of a drop at different stages of impact along with the velocity field and vorticity contours. Figure 3a–e on the left illustrates the drop morphology through high speed images at different instants in time, as the drop undergoes different phases—pre-impact phase, post-impact spreading, upward recoil, downward recoil and decay, respectively. Figure 3f–i on the right show the corresponding internal velocity fields at different stages of drop motion. During the pre-impact phase (Fig. 3a), the initially spherical drop produced by the syringe transitions into an oblate spheroid by the action of gravity. This effect is predominantly observed in drops of larger sizes (Pruppacher and Beard 1971). Correspondingly, Fig. 3f shows the velocity field with the velocity of the drop centroid subtracted from the entire velocity field to indicate the negligible internal motion in the pre-impact phase. Upon impact, the drop spreads radially outwards (Fig. 3b) and forms a very thin flattened disk shape and momentarily comes to rest. At this location of the maximum spreading, the average initial kinetic energy of the drop manifests in the form of increased surface energy and the inertia forces are balanced by the surface tension forces. The velocity field inside the drop during this phase is difficult to be quantified because of the excessive refraction occurring at the interface. Due to the effect of surface tension forces, the drop then recoils inwards and upwards, with a consequent increase in kinetic and gravitational potential energy and a simultaneous reduction in surface energy (Fig. 3c). The corresponding internal flow field at this phase, as illustrated in Fig. 3g, demonstrates a strong net upward motion, with two distinct, opposite vortex cores on either sides of the drop centroid. This flow pattern represents a vortex ring similar to that

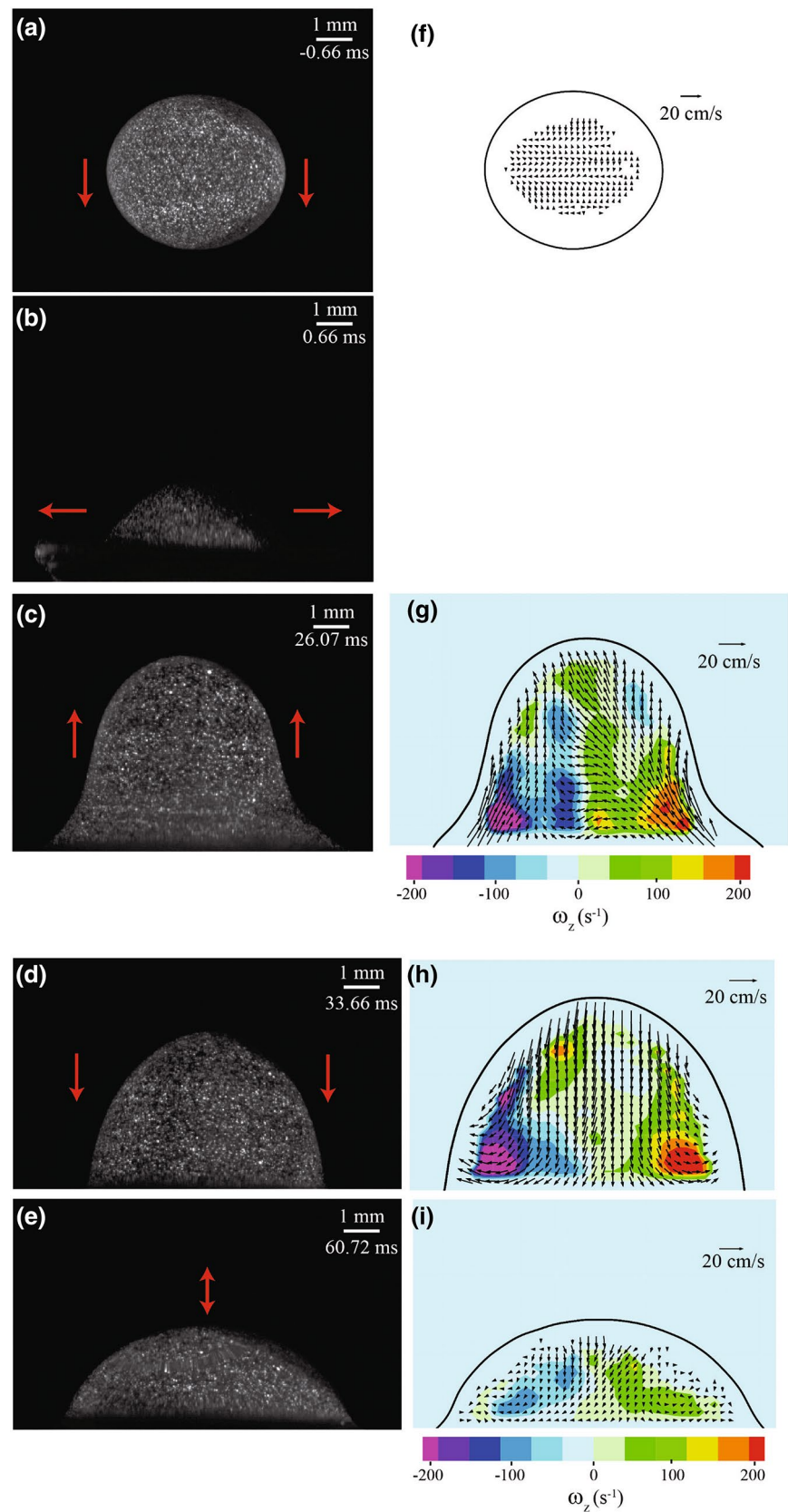
observed by Mohamed-Kassim and Longmire (2003) in drop impacts on a liquid–liquid interface. A further interplay between the kinetic and gravitational potential energy leads the drop to recoil to a maximum height and then back downwards (Fig. 3d). Correspondingly, the flow field during this phase shows vortex cores persisting with a net downward velocity (Fig. 3h). The drop then continues its vertical oscillations with diminishing amplitudes (Fig. 3e) until the motion decays away under the effect of dissipative forces. Figure 3i demonstrates a considerable reduction in vorticity in the internal flow field during this decay phase.

#### 3.2 Variation of internal vortex pattern upon different pre-impact conditions

Internal flow measurements have been conducted under different pre-impact conditions, characterized by impact number  $P$ . Depending on the impact number, different vortex modes are observed in the recoil phase of the drop impact. Figure 4a–c shows the time-averaged internal velocity field of the drop, overlaid on the time-averaged absolute vorticity magnitude,  $|\omega_z|$  contours, during the end of the upward recoil phase. This time averaging includes 11 instantaneous vector fields, 5 on either side of the maxima in  $y$ -position, chosen specifically due to the minimal change in drop geometry. The total recoil durations range from 20 to 25 ms, and do not show any systematic dependence upon  $P$ , in the range of impact conditions tested. As Fig. 4a illustrates, at a lower  $P$  (e.g.,  $P=0.10$ ), two distinct vortex cores are observed at the bottom corners of the drop. Though the drop is not perfectly symmetric, these vortices indicate a vortex ring and the vortex pattern is referred to as single ring (SR). With a gradual increase in  $P$  (e.g.,  $P=0.29$ ), an additional vortex ring is observed above the primary vortex ring, near the top of the drop (Fig. 4b). The vorticity of this vortex ring is negative and significantly lower than that of the primary ring. With a further increase in  $P$  (e.g.,  $P=0.36$ ), the vorticity magnitude of the secondary vortex ring increases to equal that of the primary ring (Fig. 4c) with the maximum vorticity magnitude lower than in the single ring case. This vortex pattern is referred to as double ring (DR). Note that due to the asymmetry of the drop, the positive vorticity of the second ring vortex is of lower magnitude compared to its negative value.

Based on our measurements and observations, the vortex pattern is reasoned to originate during the spreading phase of the drop's motion. At impact, the liquid at the bottom of the drop comes to rest and the inertia of the liquid in motion forces the stagnant liquid radially outwards, leading to the spreading of the drop. At the drop's periphery, surface forces stop the radial spreading and cause the liquid to recirculate inwards, giving rise to vortical motion inside the drop as shown in Fig. 5a. It is

**Fig. 3** A sample sequence of original particle tracer images showing **a** the pre-impact, **b** the post-impact spreading, **c** upward recoil, **d** downward recoil, and **e** decay phases during a drop impact process. The corresponding instantaneous velocity fields overlaid on the vorticity contours and detected droplet shape of **f** the pre-impact, **g** upward recoil, **h** downward recoil, and **i** decay phases. The *red arrows* indicate the bulk motion of the drop surface.  $P$  in this impact is 0.28 and the liquid used is mixture III. Note that in the image sequence, the time-stamps indicate time from the moment of impact



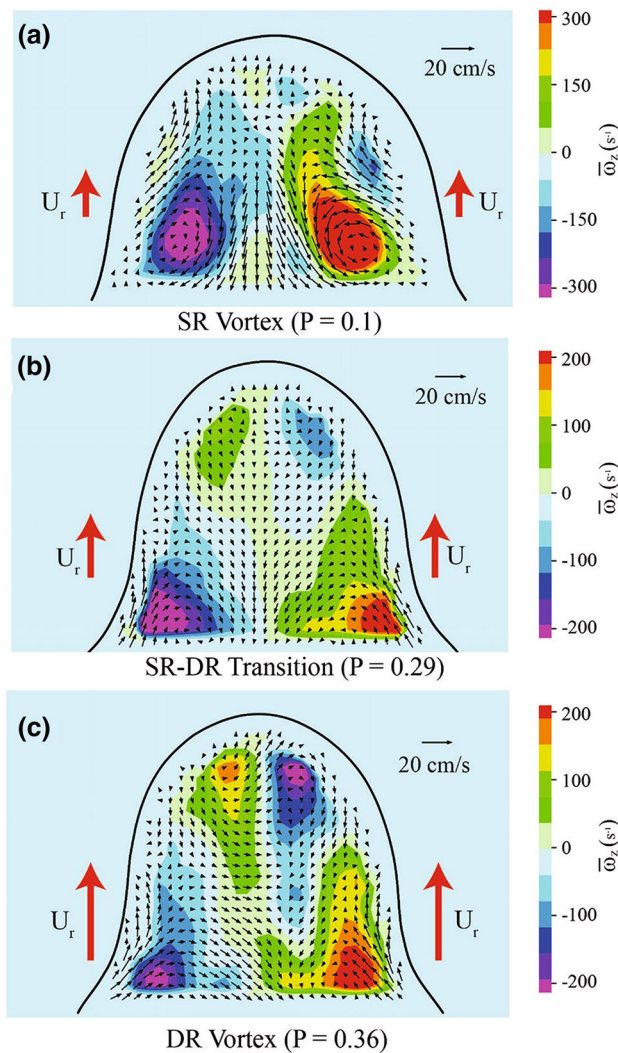


**Fig. 4** The time-averaged velocity field overlaid on the vorticity contours during the recoil phase for a 4 mm, 30% aqueous glycerin drop at **a**  $P = 0.10$ , **b**  $P = 0.29$ , **c**  $P = 0.36$

evident that the vorticity should depend upon an interplay between the spreading and recoil velocities, and liquid properties such as viscosity. Our high-speed videos and measurements indicate the occurrence of a similar phenomenon explaining the underlying cause behind the transition from SR to DR mode for a particular liquid. Essentially, as  $P$  increases for a given liquid, the resulting increase in the impact kinetic energy leads to a greater spreading, and subsequently larger vertical recoil velocity. The higher vertical recoil velocity,  $U_r$ , causes the bulk liquid to move upwards (Fig. 5c) till it reaches the drop periphery at the top. A phenomenon similar to the formation of primary vortex ring caused by spreading in the radial direction, occurs in the transverse direction this time, causing the liquid to recirculate downwards

(Fig. 5d) and form another vortex ring as shown in Fig. 5e. Note that because of this induced recirculation at the drop periphery on the top, the secondary vortex ring is opposite in sense as compared to the primary vortex ring as shown in Fig. 4c.

### 3.3 Vortex strength and internal kinetic energy under different pre-impact conditions

The dependence of the vortex strength inside the drop upon the impact number is further investigated for a series of experiments with different liquid mixtures. To obtain a wide range of  $P$ , each liquid viscosity, highlighted in Table 1, is used in combination with three different needle diameters and varying pre-impact velocities. To characterize and compare the strength of the vortices under these different impact conditions, the time-averaged absolute vorticity magnitude during the end of the upward recoil phase,  $|\omega_z|$ , is spatially averaged over the vortex cores and is designated  $\langle |\omega_z| \rangle$ . Specifically, the area of the vortex core is defined by the portion of the drop where the vorticity is greater than 50% of the maximum vorticity magnitude. Figure 6 shows the variation of this non-dimensionalized vortex strength, i.e.  $|\tilde{\omega}_z| = \langle |\omega_z| \rangle / (U_0/D_0)$ , with  $P$  for different liquid mixtures. As shown the vortex strength decreases with an increase in  $P$  and shows a least-squares, negative power law correlation with an exponent of  $-0.89$ . This inverse power law relationship between vortex strength and impact number is clearly illustrated by the reduction in vorticity magnitude when we make a transition from a SR to a DR vortex mode due to an increase in  $P$  (Fig. 4). It can be shown that vortex strength should follow a negative power law scaling with respect to  $P$  (since  $P \propto U_0^6/D_0^5$  according to the definition of impact number), with an exponent of  $-5/6$ , close to the exponent obtained from the fitting.

Further, the energy due to the internal motions initiated within a drop upon impact is also explored at the end of the upward recoil where this internal kinetic energy (IKE) would be maximum. To quantify the IKE, we subtract the energy due to the motion of the centroid from the kinetic energy calculated from PIV and non-dimensionalized as  $I\tilde{K}E = IKE/KE_0$ , where  $KE_0$  is the pre-impact kinetic energy of the drop. Figure 7 shows the variation of  $I\tilde{K}E$  with  $P$  for the aforementioned data sets used to quantify the vortex strength. A similar negative power law correlation with respect to  $P$ , with an exponent of  $-1.13$  is observed. It is worth noting that the bulk kinetic energy ratio in the recoil phase and in the pre-impact phase is of the order of  $10^{-2}$ . This substantial decrease in kinetic energy can be attributed to viscous dissipation during the spreading phase and due to increase in surface energy caused by the change in the drop's geometry. This implies that the ratio of  $I\tilde{K}E$  to the bulk kinetic energy ranges from 2%, for lower impact

**Fig. 5** Schematics illustrate **a** the formation of flow patterns during the spreading phase, **b** inward horizontal recoil leading to SR, **c** vertical recoil leading to upward motion of the bulk liquid which marks the beginning of recoil phase, **d** recirculation of liquid at the top drop surface, **e** formation of DR with the drop being stationary marking the end of upward recoil, **f** downward motion of the bulk liquid, **g** both downward and horizontal motion of bulk liquid, and **h** decay phase

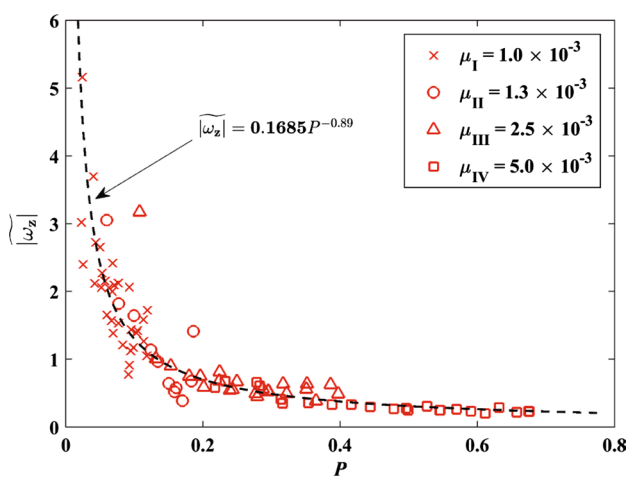
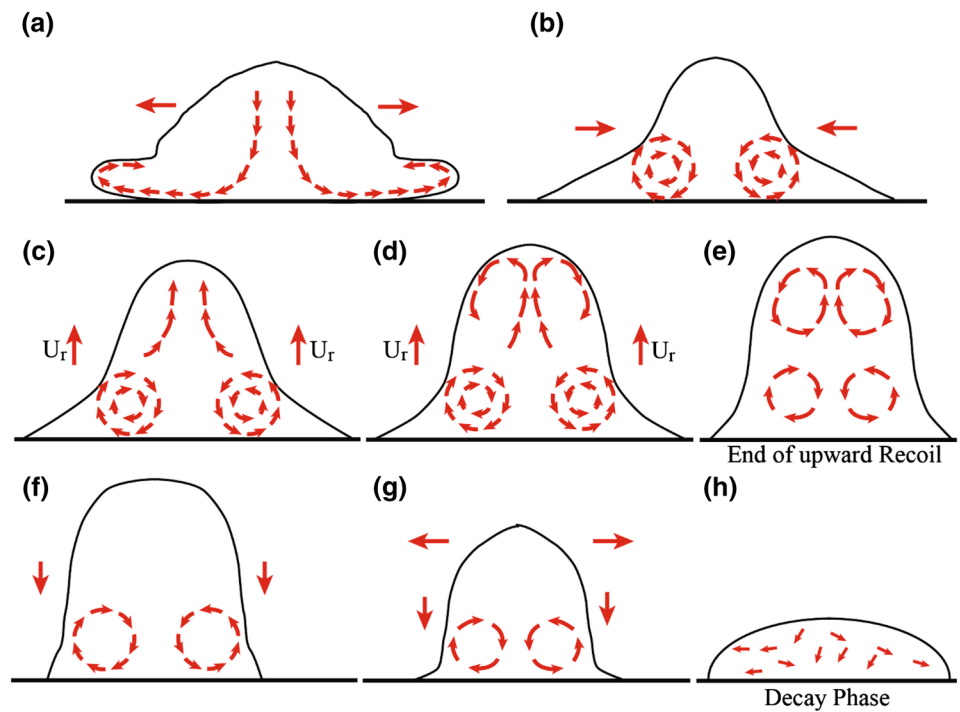


**Fig. 6** The dependence of vortex strength upon impact number  $P$ , during the end of upward recoil phase for drops of varying dynamic viscosity. The dashed lines indicate a negative power law fit to the experimental data. The  $R^2$  value for the fit is 0.9913

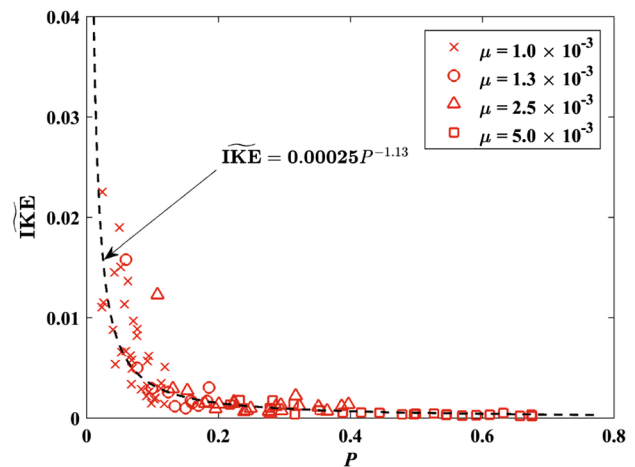


**Fig. 7** The dependence of time-averaged internal kinetic energy upon impact number  $P$ , during the end of upward recoil phase for drops of varying dynamic viscosity. The dashed lines indicate a negative power law fit to the experimental data. The  $R$ -square value for the fit is 0.9857

numbers, to 0.02%, for higher impact numbers. This is particularly significant in understanding the mixing characteristics of drop impacts as the criterion for pinch off to form a secondary droplet which is speculated to be influenced by the internal motions.

From Fig. 7 it is evident that  $IKE$  is inversely proportional to  $P$ . This result is reasonable as  $P$  increases with

an increase in dynamic viscosity. Considering the viscosity of the drop is positively correlated to its resistance to deformation, drops with higher viscosity (hence higher  $P$ ) deform less during the spreading phase of the impact. Since the internal kinetic energy is generated during the spreading phase, an impact with a higher  $P$  will have a lower internal kinetic energy.



## 4 Conclusion

Particle imaging velocimetry studies using fluorescent tracers are conducted on the plane of symmetry of liquid drops as they impact a hydrophobic surface. An algorithm is developed to correct the geometrical optical distortion caused by the curved drop surface. Using the corrected images, the velocity field within the drop is visualized and distinct vortices are observed. Further, depending on the impact number we see two different modes of vortices, single ring and double ring, where the transition between the two modes is facilitated by increasing the liquid's viscosity. The vortex strength was found to scale with impact number as  $0.1685P^{-0.89}$  and the maximal internal kinetic energy of the liquid motion within the drop was found to scale with impact number as  $I\tilde{K}E \propto P^{-1.13}$ . It is expected that the internal kinetic energy will be more significant for drops falling in a more viscous fluid as reported in Mohamed-Kassim and Longmire (2003) and in Ninomia and Yasuda (2006). In addition, even a few percent change in drop kinetic energy during impact could lead to significantly different post impact behaviors as pointed in a recent study by Howland et al. (2016). This study shows that only a few percent difference in the kinetic energy dissipation was leading to an absence of splashing on the flexible surfaces compared to the rigid cases at similar impact conditions. These results further reinforce the significance of internal motions initiated within a droplet with regard to post-impact drop geometry, pinch off to form satellite droplets, mixing characteristics, etc., which needs to be further investigated.

**Acknowledgements** This work is supported by Office of Naval Research–United States under Grant # N000140910141 (Program manager: Dr. Ronald Joslin) and Grant # 12044075 (Program manager: Dr. Thomas Fu), and the startup of Jiarong Hong from the University of Minnesota.

## References

- Agbaglah G, Thoraval MJ, Thoroddsen ST, Zhang LV, Fezzaa K, Deegan RD (2015) Drop impact into a deep pool: Vortex shedding and jet formation. *J Fluid Mech* 764:1. doi:10.1017/jfm.2014.723
- Attinger D, Moore C, Donaldson A, Jafari A, Stone HA (2013) Fluid dynamics topics in bloodstain pattern analysis: Comparative review and research opportunities. *Forens Sci Int* 231.1:375–396
- Bernardin JD, Clinton JS, Mudawar I (1996) Effects of surface roughness on water droplet impact history and heat transfer regimes. *Int J Heat Mass Transfer* 40.1:73–88
- Chandra S, Avedisian CT (1991) On the collision of a droplet with a solid surface. *Proc R Soc Lond A Mat* 432.1884:13–41
- Clanet C, Béguin C, Richard D, Quéré D (2004) Maximal deformation of an impacting drop. *J Fluid Mech* 517.1:199–208
- Glycerine Producers (1963) Association physical properties of glycerine and its solutions. Glycerine Producers' Association, New York
- Howland J.C, Antkowiak A, Castrejon-Pita R, Howison S.D, Oliver J.M, Style R.W, Castrejon-Pita A.A (2016) Its harder to splash on soft solids. *PRL* 117:184502–1:5
- Hulse S, Lee, Illes M (2007) A blind trial evaluation of a crime scene methodology for deducing impact velocity and droplet size from circular bloodstains. *J Forens Sci* 52.1:65–69
- Lee JS, Weon BM, Je JH, Fezzaa K (2012) How does an air film evolve into a bubble during drop impact? *Phys Rev Lett* 109.20:204501
- Li EQ, Thoroddsen ST (2015) Time-resolved imaging of a compressible air disc under a drop impacting on a solid surface. *J Fluid Mech* 780.1:636–648
- Minor G, Oshkai P, Djilali N (2007) Optical distortion correction for liquid droplet visualization using the ray tracing method: further considerations. *Meas Sci Tech* 18.11:23–28
- Mohamed-Kassim Z, Longmire EK (2003) Drop impact on a liquid–liquid interface. *Phys Fluids* 15.11:3263–3273
- Ninomiya N, Yasuda K (2006) Visualization and PIV measurement of the flow around and inside of a falling droplet. *J Vis* 9.3:257–264
- Pruppacher HR, Beard KV (1971) A wind tunnel investigation of the internal circulation and shape of water drops falling at terminal velocity in air. *Q J R Meteorol Soc* 97.411:133–134
- Rieber M, Frohn A (1999) A numerical study on the mechanism of splashing. *Int J Heat Fluid Flow* 20.5:455–461
- Rioboo R, Tropea C, Marengo M (2001) Outcomes from a drop impact on solid surfaces. *At Sprays* 112:155–165
- San Lee J, Park SJ, Lee JH, Weon BM, Fezzaa K, Je JH (2015) Origin and dynamics of vortex rings in drop splashing. *Nat Commun* 6.doi:10.1038/ncomms9187
- Sharma PP, Gupta SC, Foster GR (1995) Raindrop-induced soil detachment and sediment transport from interrill areas. *Soil Sci Soc Am J* 59.3:727–734
- Thoraval MJ, Takehara K, Etoh TG, Popinet S, Ray P, Josserand C, Thoroddsen ST (2012) von Kármán vortex street within an impacting drop. *Phys Rev Lett* 108 0.26:264506
- Thoraval MJ, Takehara K, Etoh TG, Thoroddsen ST (2013) Drop impact entrapment of bubble rings. *J Fluid Mech* 724.1 :234–258
- Thoroddsen ST, Etoh TG, Takehara K (2003) Air Entrapment under an impacting drop. *J Fluid Mech* 478.1:125–134
- Weiss DA, Yarin AL (1999) Single drop impact onto liquid films: Neck distortion, jetting, tiny bubble entrainment, and crown formation. *J Fluid Mech* 385.1 :229–254
- Xu L, Zhang WW, Nagel SR (2005) Drop splashing on a dry smooth surface. *Phys Rev Lett* 94.18:184505
- Yarin AL (2006) Drop impact dynamics: splashing, spreading, receding, bouncing and helling. *Annu Rev Fluid Mech* 38.1:159–192
- Yarin AL, Weiss DA (1995) Impact of drops on solid surfaces: self-similar capillary waves, and splashing as a new type of kinematic discontinuity. *J Fluid Mech* 283.1:141–173
- Zhang LV, Toole J, Fezzaa K, Deegan RD (2012) Evolution of the ejecta sheet from the impact of a drop with a deep pool. *J Fluid Mech* 690.1 :5–15
- Zhao R, Zhang Q, Tjugoito H, Cheng X (2015) Granular impact cratering by liquid drops: understanding raindrop imprints through an analogy to asteroid strikes. *Proc Natl Acad Sci* 112(2):342–347